Cement and Concrete Composites 171 (2026) 106643

Contents lists available at ScienceDirect

Cement and Concrete Composites

journal homepage: www.elsevier.com/locate/cemconcomp

Pull-out behaviour of single and multiple hooked-end steel fibres embedded in alkali-activated slag-based concrete and Portland cement concrete: Experimental and numerical investigation

Laura Rossi [a,b,*], Maria Paula Zappitelli [c], Ravi A. Patel [a,b], Frank Dehn [a,b]

[a] Institute of Building Materials and Concrete Structures (IMB), Karlsruhe Institute of Technology (KIT), 76131, Karlsruhe, Germany
[b] Materials Testing and Research Institute Karlsruhe (MPA), Karlsruhe Institute of Technology (KIT), 76131, Karlsruhe, Germany
[c] Department of Civil Engineering, Engineering College, National University of La Plata (UNLP), Street 1 and 47, La Plata, Argentina

ARTICLE INFO

Keywords:
Alkali-activated concrete
Hooked-end steel fibres
Pull-out behaviour
Finite element modelling
Cohesive zone model
Inverse analysis

ABSTRACT

This paper investigates the 7-day and 28-day pull-out behaviour of single (3D), double (4D), and triple hooked-end steel fibres (5D) embedded in alkali-activated slag-based concrete (AASC) and Portland cement-based concrete (PCC). Experimental results indicate that both the maximum pull-out load and the average fibre-matrix bond strength increase with the number of bends at the fibre ends, with AASC consistently outperforming PCC, confirming a stronger fibre-matrix interfacial bond strength in the alkali-activated system. An inverse analysis was performed to identify the interface Cohesive Zone Model (CZM) parameters implemented in ABAQUS using data obtained from the experimental single-fibre pull-out tests. The parameters governing the initial slope and the maximum pull-out load (interface stiffness and traction stress, respectively), as well as those controlling the post-peak behaviour (separation and friction coefficients), were identified. The results show that the interface stiffness parameter increases with the number of bends at the fibre ends, and the fibre-matrix bond fracture energy, derived from the traction stress and separation, was highest for double hooked-end (4D) fibres, which also exhibited the highest fibre material utilisation factor. Finally, by combining the average fibre-matrix bond strength with the number of fibres in the cross-section of notched beams tested under three-point bending, a linear relationship was established between single-fibre pull-out behaviour and residual flexural strengths at serviceability and ultimate limit states.

1. Introduction

Portland cement-based concrete (PCC) is inherently brittle and prone to sudden tensile failure. To mitigate this, randomly distributed steel fibres are often incorporated into the cementitious matrix, as they enhance the tensile response by bridging cracks and thereby delaying their initiation and propagation [1]. The efficiency of this mechanism depends on the properties of the concrete matrix, the characteristics of the fibres, and the strength of the fibre-matrix interfacial bond. A weak bond leads to premature fibre pull-out under relatively low loads, while an excessively strong bond may cause fibre rupture [1], [2]. Hence, an optimal fibre-matrix bond strength is required to ensure fibre deformation, effective stress transfer, and controlled pull-out while preventing sudden fibre slip or rupture.

The mechanisms governing the fibre-matrix bond include electrostatic attraction, chemical adhesion, and, most importantly, mechanical interlocking, which is strongly influenced by the fibre geometry. Compared to straight fibres, hooked-end steel fibres exhibit greater fibre-matrix interfacial bond strength and pull-out toughness due to the enhanced anchorage provided by their more complex geometry [1], [3], [4]. An increase in the number of bends at the fibre ends has been demonstrated to further improve the fibre-matrix bond and maximum pull-out load [5], leading to the development and commercialisation of double (4D) and triple (5D) hooked-end steel fibres. These fibres lead to superior post-cracking tensile performance at lower dosages compared to conventional single (3D) hooked-end steel fibres [6], [7].

Single-fibre pull-out tests are widely used to assess the fibre-matrix interfacial bond strength [8]. Fig. 1 shows a typical pull-out-slip curve for a single hooked-end steel fibre, which may generally be divided into 5 stages. Stage I ($\delta < \delta_1$) represents the purely elastic phase, during

* Corresponding author. Institute of Building Materials and Concrete Structures (IMB), Karlsruhe Institute of Technology (KIT), 76131, Karlsruhe, Germany.
E-mail addresses: laura.rossi@kit.edu (L. Rossi), paula.zappitelli@ing.edu.ar (M.P. Zappitelli), ravi.patel@kit.edu (R.A. Patel), frank.dehn@kit.edu (F. Dehn).

https://doi.org/10.1016/j.cemconcomp.2026.106643
Received 1 October 2025; Received in revised form 20 January 2026; Accepted 21 April 2026
Available online 28 April 2026

which the fibre remains fully bonded to the matrix and the adhesion between the fibre and the concrete matrix governs its deformation [3]. Fibre debonding begins at the end of the linear portion of the curve ($\delta_1 < \delta < \delta_2$) during which the fibre's hooked end undergoes bending and plastic deformation, thereby increasing the pull-out load to its maximum value (P_2) and forming two inelastic hinges (H_1 and H_2) [3], [4]. Once the load reaches its maximum, the straightening of the fibre's end begins. Hinge H_2 disappears and the pull-out load decreases until the final portion of the fibre hooked end is forced to bend in the opposite direction from its original shape through the second angle of the fibre-matrix interface. This produces a second peak followed by a drop in the pull-out load ($\delta_2 < \delta < \delta_3$). In Stage IV ($\delta_3 < \delta < \delta_4$), hinge H_1 also disappears and complete debonding is achieved at $\delta = \delta_4$ [3]. In the final stage, Stage V ($\delta > \delta_4$), the fibre is essentially straight and the pull-out resistance is provided only by frictional sliding along the fibre embedded length. Once the fibre is completely pulled out the concrete matrix ($\delta = L_e$), the pull-out load drops to zero ($P_{\delta=L_e} = 0$) [3], [4]. If the deformed hooked ends of the fibre do not undergo yielding, fibre rupture may occur [9]. For double (4D) and triple (5D) hooked-end steel fibres, additional plastic hinges form during the fibre pull-out (Fig. 1), resulting in supplementary load peaks in the pull-out slip curve prior complete fibre pull-out and greater energy absorption [8]. In the case of 5D fibres, the enhanced mechanical anchorage provided by the fibre geometry, combined with the higher tensile strength of the wire, allows significant fibre elongation; consequently, fibre rupture may become the dominant failure mechanism, in contrast to the pull-out failure typically observed for 3D and 4D fibres.

While the pull-out behaviour of single (3D) hooked-end steel fibres has been extensively investigated, with findings demonstrating that the main influencing factors are the mechanical deformation of the fibre and the strength of the concrete matrix [8], the mechanisms governing the pull-out response of 4D and 5D fibres have only recently begun to be investigated, owing to their novelty and the advantages they offer over 3D fibres in terms of the composite's mechanical performance. Abdallah et al. [8] investigated the pull-out behaviour of 3D, 4D and 5D fibres embedded in ultra-high-performance cement-based mortar to evaluate the mechanical anchorage provided by the additional bends at the fibre ends. During pull-out, the fibre bends are idealised as two, three and four plastic hinges for 3D, 4D and 5D fibres, respectively. Therefore, the mechanical anchorage provided by these additional bends is directly related to the energy required to straighten the fibres during pull-out. Abdallah et al. [10] also demonstrated experimentally that the hooked ends of 4D and 5D fibres were only partially deformed and straightened when embedded in normal-strength cement-based concrete, suggesting that increased concrete matrix strength enhances the pull-out performance of hooked-end steel fibres [11]. Another parameter affecting the pull-out response of both single and multiple hooked-end steel fibres is the fibre embedment length, as both the maximum pull-out load and the pull-out work increase with increased embedded length [12].

Although the pull-out behaviour of 3D, 4D and 5D fibres embedded in cement-based mortar and concrete has been evaluated by several authors [8], [10], [13], [14], [15], studies on their performance in alternative cement-free binders, such as alkali-activated slag-based concrete (AASC), remain limited. Beglarigale et al. [16] evaluated the fibre-matrix bond strength of 3D fibres in alkali-activated slag-based mortar and compared it with cement-based mortar and ultra-high performance cement-based concrete (with a maximum aggregate size of 4 mm). Their results demonstrated that alkali-activated slag-based mortar exhibits superior fibre-matrix bond characteristics compared to cement-based mortar, achieving a higher maximum pull-out load even at lower matrix compressive strength values than cement-based composites. Shaikh [5] evaluated the pull-out behaviour of 3D, 4D and 5D steel fibres in fly ash-slag blended alkali-activated mortars and traditional cement-based mortars. This study confirmed that the maximum pull-out load and the average fibre-matrix bond strength increase with the number of bends at the fibre ends, with alkali-activated mortars outperforming cement-based mortars.

Among the available numerical approaches, the Cohesive Zone Model (CZM) has emerged as a robust framework for simulating the pull-out response of fibres embedded in cementitious matrices [3], [17], [18], [19], [20], [21], [22], striking a balance between computational efficiency and predictive accuracy. Poveda et al. [17] combined cohesive and contact elements with a rate-dependent frictional law to reproduce the fibre-matrix interaction, while Fantilli and Vallini [18] employed the CZM to predict the pull-out response of inclined steel fibres. Abbas et al. [3] integrated cohesive-frictional interactions to account for hooked-end geometries, and more recently, refinements such as the inclusion of cohesive energy-related parameters by Zou and

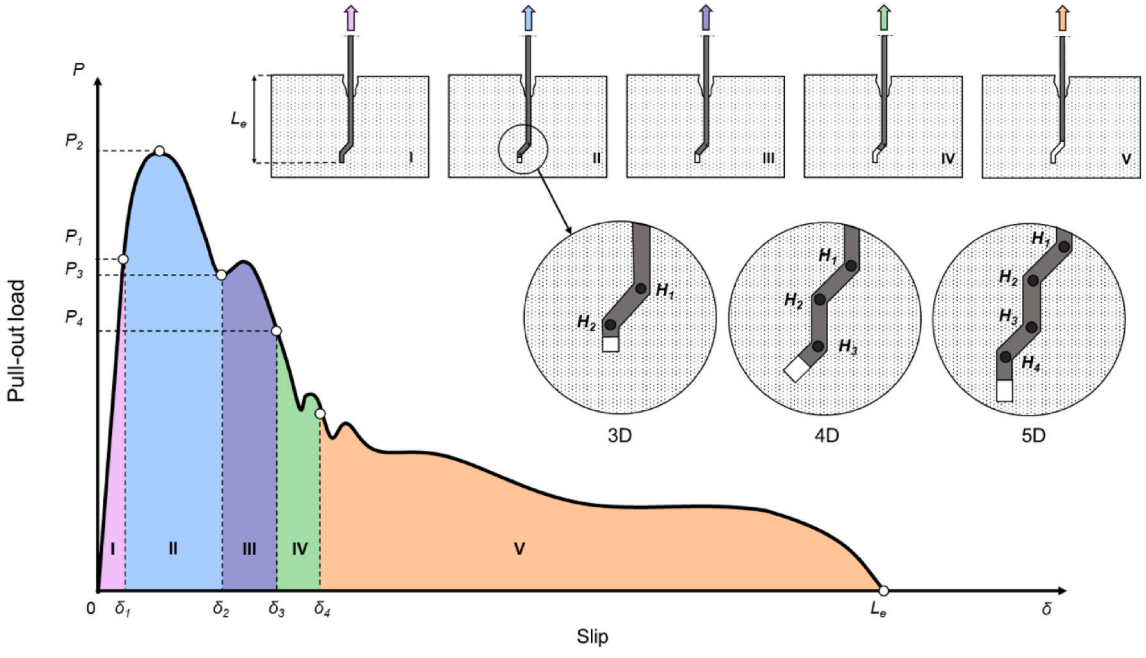

Fig. 1. Typical pull-out response of hooked-end steel fibres embedded in cement-based concrete (Modified from Refs. [3] [4]).

Hameed [19] have improved the ability of the CZM to capture both interfacial damage and frictional effects. Despite these advances, most existing CZM-based studies rely on interface parameters adopted from the literature rather than determined directly from experiments. Only a few contributions, such as those of Banholzer et al. [23] and Kožar et al. [24], have applied inverse analysis to extract bond-slip parameters from experimental pull-out data.

Despite the recent increase in research interest in steel fibre-reinforced alkali-activated slag-based composites, existing experimental studies have predominantly focused on evaluating the single-fibre pull-out behaviour of single (3D) and multiple (4D, 5D) hooked-end steel fibres in mortar-scale specimens. Furthermore, current numerical studies employing the Cohesive Zone Model (CZM) are largely limited to cement-based concrete, with fibre-matrix interface parameters commonly adopted from the literature rather than derived from experiments. In addition, the relationship between single-fibre pull-out behaviour and the flexural response of AASC incorporating single and multiple hooked-end steel fibres at different volume fractions remains unexplored. To address these aspects, this study experimentally investigates the single-fibre pull-out behaviour of single (3D), double (4D), and triple (5D) hooked-end steel fibres embedded in both alkali-activated slag-based concrete (AASC) and Portland cement-based concrete (PCC) at curing ages of 7 and 28 days. An inverse analysis framework coupled with the CZM is employed to directly derive the fibre-matrix interface parameters governing the bond-slip behaviour from single-fibre pull-out tests. This dual experimental-numerical approach provides a more accurate representation of the fibre-matrix bond strength in both AASC and PCC, enhancing the predictive reliability of numerical simulations and extending the applicability of the CZM beyond conventional cement-based concrete matrices.

2. Experimental programme

2.1. Materials

Ground granulated blast furnace slag (GGBFS) and Portland cement (CEM I 42.5 R), supplied by Ecocem Benelux B.V. and Heidelberg Materials, respectively, were used as binders in this study. Their chemical compositions are given in Table 1. Sodium hydroxide (SH) and sodium silicate (SS) were combined with water to prepare an alkaline solution with a silicate modulus $M_{s(sol)}$ of 0.5 [mol/mol], defined as the molar ratio between SiO_2 and Na_2O, and a total Na_2O concentration of 5.3 [g/100g GGBFS]. River sand and quartzite gravel were used as the fine and coarse aggregates, respectively.

Single (3D), double (4D), and triple (5D) hooked-end steel fibres, each 60 mm in length and 0.90 mm in diameter, were supplied by NV Bekaert SA. The three fibre types investigated in this study – Dramix® 3D 65/60 BG, Dramix® 4D 65/60 BG, and Dramix® 5D 65/60 BG – differ primarily in the number of bends at the fibre ends and the tensile strength of the wire. Their key properties are summarised in Table 2.

2.2. Mix proportions

Table 3 shows the mix proportions used for alkali-activated slag-based concrete (AASC) and Portland cement-based concrete (PCC). Both mixtures employed the same binder content, aggregate type, and aggregate content. This ensured comparable slump flow class (F4) and 28-day mean compressive strength, which was evaluated on three 150 mm × 150 mm x 150 mm cubes.

Table 2
Hooked-end steel fibres properties.

Fibre type	Length (l_f) [mm]	Diameter (d_f) [mm]	Aspect ratio (l_f/d_f)	Hook length [mm][a]	Fibre tensile strength (σ_{tf}) [MPa]	Strain at ultimate strength [%]
3D 65/60 BG	60	0.90	65	4.76	1160	0.8
4D 65/60 BG	60	0.90	65	7.55	1600	0.8
5D 65/60 BG	60	0.90	65	10.24	2300	6.0

[a] Calculated from [12].

2.3. Specimen preparation

A prismatic steel mould with dimensions 500 mm × 80 mm x 50 mm, designed to accommodate six single fibres at regular intervals, was used for each fibre type and concrete matrix. The fibres were positioned in the mould prior to casting to ensure an embedded length of 15 mm. Fresh concrete was poured into the mould in a single layer and carefully compacted by hand to prevent fibre displacement. After 24 h, the samples were demoulded, and each beam was sawed to obtain six samples with final dimensions of 80 mm × 80 mm x 50 mm, as illustrated in Fig. 2. Following sawing, the 72 samples – six for each combination of fibre geometry, concrete matrix and testing age – were wrapped in foil and stored at (20 ± 2) °C until testing age to prevent corrosion of the exposed fibres.

Additionally, twelve cubes (150 mm × 150 mm x 150 mm) were cast to evaluate the mean compressive strength of the plain concrete matrices at 7 and 28 days, in accordance with EN 12390-3.

2.4. Single-fibre pull-out test setup

Fig. 3 shows the pull-out test setup used in this study. The test was displacement-controlled, with a constant loading rate of 10 mm/min and an initial preload of 5 N. The elastic elongation of the fibre during the testing was neglected.

From each experimental load-displacement (slip) curve, the maximum pull-out load (P_{max}), the average fibre-matrix bond strength (τ_{avg}), the equivalent bond strength (τ_{eqv}) and the fibre material utilisation factor (*FMUF*) were determined according to Eq. (1) – Eq. (3) [5], using an embedment length (L_e) of 15 mm.

$$\tau_{avg} = \frac{P_{max}}{\pi d_f L_e} \tag{1}$$

$$\tau_{eqv} = \frac{2W_p}{\pi d_f L_e^2} \tag{2}$$

$$FMUF = \frac{\sigma_{t,max}}{\sigma_{tf}} \tag{3}$$

where P_{max} is the maximum pull-out load, d_f is the fibre diameter, L_e is

Table 1
Chemical composition of GGBFS and CEM I used in this study.

Binder	CaO [%]	SiO_2 [%]	Al_2O_3 [%]	Fe_2O_3 [%]	MgO [%]	P_2O_5 [%]	K_2O [%]	Na_2O [%]
GGBFS	41.84	35.91	10.74	0.39	6.99	0.47	0.40	0.31
CEM I	60.80	19.60	5.25	2.38	1.53	0.13	0.80	0.10

Table 3
Mix proportions for AASC and PCC in kg/m^3. The values in the brackets are the standard deviation from the mean value of the compressive strength.

Mix	GGBFS	CEM I	SH	SS	Water	Sand (0-2 mm)	Fine aggregates (2-8 mm)	Coarse aggregates (8-16 mm)	7-day CS [MPa]	28-day CS [MPa]
AASC	425	-	50	36	154	660	495	495	36.6 (0.38)	50.2 (0.44)
PCC	-	425	-	-	229	660	495	495	41.3 (0.78)	49.5 (0.79)

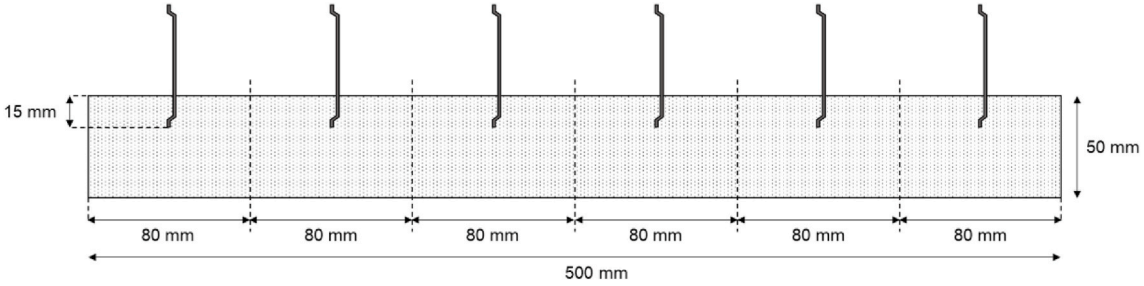

Fig. 2. Schematic representation of the single-fibre pull-out samples. The dashed lines represent the sawing locations.

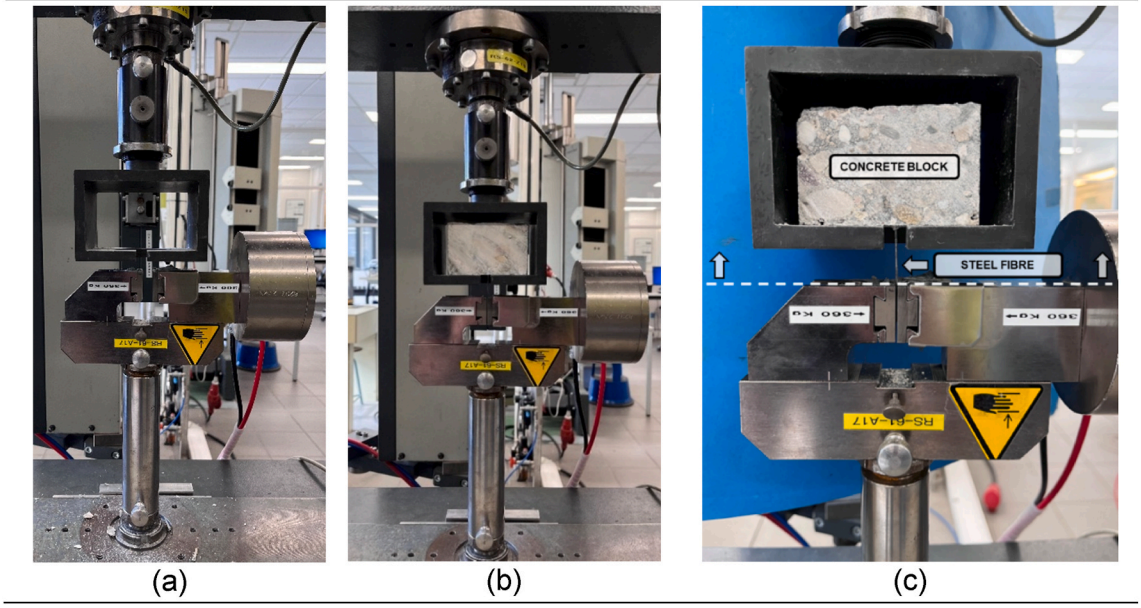

Fig. 3. Single fibre pull-out setup.

Table 4
Values of N_f, f_{R1}, and f_{R3} for each type of matrix and fibre. The values in the brackets represent the standard deviation from the average value of N_f

Matrix type	Fibre type	Fibre dosage [kg/m^3]	Experimental N_f	Predicted N_f	Ratio predicted/experimental	f_{R1} [MPa]	f_{R3} [MPa]
AASC	3D	20	56 (9.8)	44	0.786	2.93	3.45
		40	115 (12.4)	87	0.757	5.66	6.93
		60	151 (25.0)	131	0.866	6.88	8.03
	4D	20	50 (10.2)	44	0.880	3.15	3.91
		40	86 (15.6)	87	1.012	5.55	6.91
		60	152 (21.4)	131	0.862	7.86	8.05
	5D	20	39 (9.2)	44	1.128	2.44	3.07
		40	99 (18.3)	87	0.879	6.23	7.88
		60	152 (22.2)	131	0.862	7.66	8.30
PCC	3D	20	42 (7.3)	44	1.048	2.88	3.05
		40	87 (23.1)	87	1.000	5.41	6.07
		60	122 (22.5)	131	1.074	6.34	7.28
	4D	20	44 (8.5)	44	1.000	2.81	4.14
		40	76 (11.7)	87	1.145	5.53	7.05
		60	105 (20.6)	131	1.248	6.16	6.66
	5D	20	42 (6.8)	44	1.048	3.11	4.27
		40	96 (15.5)	87	0.906	5.10	5.98
		60	91 (10.4)	131	1.440	8.23	8.73

the embedded length of the fibre and W_p is the pull-out work, defined as the area under the pull-out load-displacement curve. $\sigma_{t,max}$ represents the tensile stress induced in the steel fibre at the maximum pull-out load, and σ_{tf} is the ultimate tensile strength of the fibre.

2.5. Three-point bending test and number of fibres at the cross-section

Three-point bending tests were performed on six notched beams, each measuring 150 mm × 150 mm x 550 mm, for every combination of concrete matrix and fibre type at different dosages (20 kg/m^3, 40 kg/m^3, and 60 kg/m^3), according to EN 14651. The resulting experimental load-CMOD (crack mouth opening displacement) curves, together with the values of the residual flexural strengths f_{R1} and f_{R3}, corresponding to CMOD values of 0.5 mm and 2.5 mm, respectively, were previously reported by the authors [7] and are summarised in Table 4.

After each bending test, each beam was completely fractured to enable manual counting of the number of fibres (N_f) in the cross-section above the notch, as shown in Fig. 4.

If manual counting of the fibres is not feasible, the number of fibres in the fracture cross-section (N_f) can be analytically estimated according to Dupont and Vandewalle [25] as follows:

$$N_f = \frac{G \cdot \alpha}{\left(\frac{\pi \cdot d_f^2}{4}\right) \cdot \rho_s} \cdot b \cdot h_{sp} \tag{4}$$

where G is the fibre dosage [kg/m^3], α is the orientation coefficient, b is the width of the beam, h_{sp} is the distance from the top of the notch to the top of the beam, d_f is the fibre diameter, and ρ_s is the density of the steel fibres.

Although the fibre embedded length (L_e) and orientation factor (α) were not directly considered in determining the experimental value of N_f, the measured values are in good agreement with the theoretical predictions obtained using the analytical expression proposed in Eq. (4), assuming $\alpha = 0.58$ from Ref. [25], $b = 150$ mm, $h_{sp} = 125$ mm, $d_f = 0.90$ mm, and $\rho_s = 7850$ kg/m^3, as presented in Table 4.

By multiplying the fibre-matrix average bond strength (τ_{avg}) by the number of fibres at the beam cross-section (N_f), the influence of fibre geometry and dosage on the composite's post-cracking residual flexural strength can be estimated. This approach allows the estimation of the residual strengths at both serviceability (f_{R1}, corresponding to a crack mouth opening displacement (*CMOD*) of 0.5 mm) and ultimate limit states (f_{R3}, corresponding to a *CMOD* of 2.5 mm).

2.6. Numerical simulations

The concrete matrix and the single (3D), double (4D), and triple (5D) hooked-end steel fibres were modelled in ABAQUS software. The bottom edge of the concrete block was constrained to prevent displacement, while a displacement of 14 mm was applied to the reference point (RP) coupled to the free end of the fibre. Boundary conditions and mesh are shown in Fig. 5.

To accurately simulate the behaviour of the different components – namely the concrete matrix, the steel fibre, and the fibre-matrix interface bond – distinct constitutive models were employed. The concrete matrix was modelled using the Concrete Damage Plasticity (CDP) model available in ABAQUS [7], [26], [27], [28]. The plasticity parameters used for the CDP model, *i.e.* σ_{b0}/σ_{c0} (the ratio of the initial biaxial compressive yield stress to the initial uniaxial compressive yield stress), K_c (shape factor, *i.e.* it represents the shape of the failure surface in the deviatoric plane), Φ (dilation angle), and e (eccentricity) were obtained for both AASC and PCC from literature [7] and are summarised in Table 5. Additionally, a trilinear tensile softening law and a trilinear damage law, with 0 denoting an undamaged state and 1 representing complete failure, were implemented as input parameters to capture the post-peak response of the material, as shown in Fig. 6. From the trilinear tensile softening law, the values of the stress at failure (σ_t) and the displacement corresponding to complete stress loss (u_{t0}) can be derived for both AASC and PCC, as shown in Table 5.

The steel fibres were modelled using an elasto-plastic constitutive law, assuming strain-hardening behaviour under uniaxial tension. The corresponding parameters are summarised in Table 6.

A critical aspect in accurately modelling the single-fibre pull-out response is the definition of the fibre-matrix interface properties. In this study, a Cohesive Zone Model (CZM), implemented via cohesive surfaces in ABAQUS, was used to simulate the fibre-matrix interaction and capture the different mechanisms involved in the single-fibre pull-out process. In the model, the fibre-matrix interface properties are represented by several key parameters: chemical adhesion is captured by the cohesive parameters (K_{ss}, t_{ss}, δ_s^f), friction resistance by the friction coefficient (μ), and mechanical anchorage by the effect of fibre geometry for each fibre type.

The CZM assumes that the interaction force between two interfaces acts as a cohesive force in a fictitious crack, thereby preventing crack propagation [29], [30]. The evolution of the cohesive stress with interface displacement is governed by a traction-separation law [31], which initially considers linear elastic behaviour, followed by damage initiation and progressive evolution [31], [32]. The elastic response is expressed as:

$$t = \begin{bmatrix} t_n \\ t_s \\ t_t \end{bmatrix} = \begin{bmatrix} K_{nn} & K_{ns} & K_{nt} \\ K_{sn} & K_{ss} & K_{st} \\ K_{tn} & K_{ts} & K_{tt} \end{bmatrix} = \begin{bmatrix} \delta_n \\ \delta_s \\ \delta_t \end{bmatrix} = K\delta \tag{5}$$

where t and δ are the nominal traction stress vector and the separation, respectively, t_n, t_s, t_t, δ_n, δ_s, and δ_t are the components of such vector in the normal (t_n, δ_n) and tangential directions (t_s, t_t; δ_s, δ_t), and K is the stiffness matrix. For the single-fibre pull-out simulation, only off-plane shear was considered (s-mode) [31], [33], leading to $K_{ns} = K_{sn} = K_{nt} = K_{tn} = K_{st} = K_{tt} = 0$ and $K_{nn} = K_{ss}$ [3]. Damage initiation, defined as the onset of stiffness degradation at the contact interface [32], is governed

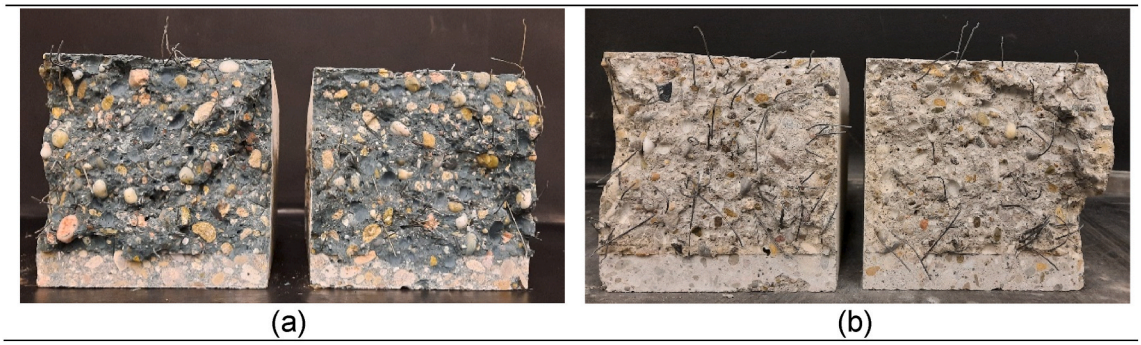

Fig. 4. Example of fractured beams for (a) alkali-activated concrete and (b) Portland cement-based concrete, used to count the number of fibres at the cross-section.

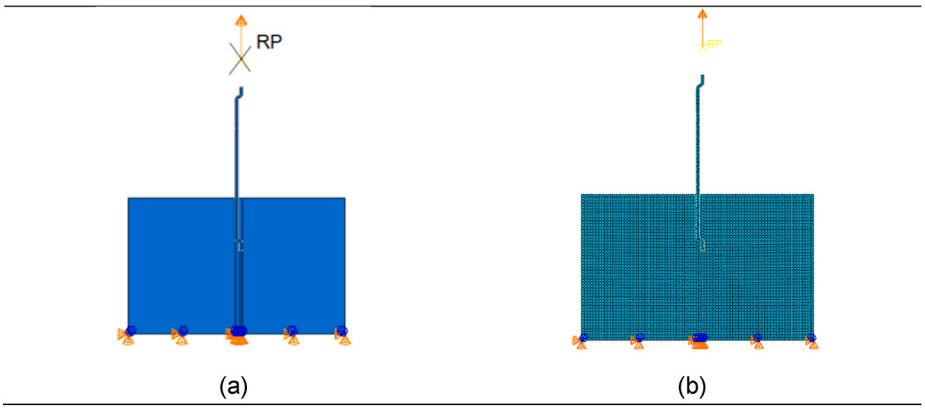

Fig. 5. Schematic representation of (a) the boundary conditions and (b) the mesh used for the numerical simulations.

Table 5
Plasticity parameters required by the CDP model and parameters describing the trilinear softening and damage law for both AASC and PCC.

Mix	σ_{b0}/σ_{c0}	K_c	Φ	e	σ_t	u_{t0}
AASC	1.16	0.6667	50°	0.1	2.19	0.118
PCC					2.46	0.208

by the quadratic stress criterion:

$$\left\{\frac{\langle t_n\rangle}{t_n^0}\right\}^2+\left\{\frac{t_s}{t_s^0}\right\}^2=1 \tag{6}$$

where t_n^0 and t_s^0 are the peak contact stresses in the normal and shear directions, respectively [32]. In this study, t_n^0 was assumed to be 10 times t_s^0, reflecting the dominance of interfacial shear slip during debonding as also previously suggested by Zhang et al. [33]. Damage evolution describes the progressive degradation of the cohesive stiffness post damage initiation [3], [32]. It characterised by a scalar damage variable (D), ranging from 0 (undamaged) to 1 (complete failure). The stress components affected by damage are given by:

$$t_n=\begin{cases}(1-D)\bar{t_n} & \bar{t_n}>0\\ \bar{t_n} & \bar{t_n}\le 0\end{cases} \tag{7}$$

$$t_s=(1-D)\bar{t_s} \tag{8}$$

where $\bar{t_n}$ and $\bar{t_s}$ are the contact stress components predicted by the elastic traction-separation law without considering damage. In this study, a linear damage law was used to define the evolution of D [19]:

Table 6
Parameters of the elasto-plastic constitutive law used for each fibre type.

Fibre type	Yield strength [MPa]	Tensile strength [MPa]	Strain at ultimate strength [%]
3D	785.05	1013.68	1.47
4D	1121.21	1443.94	2.42
5D	1912.87	2225.96	6.82

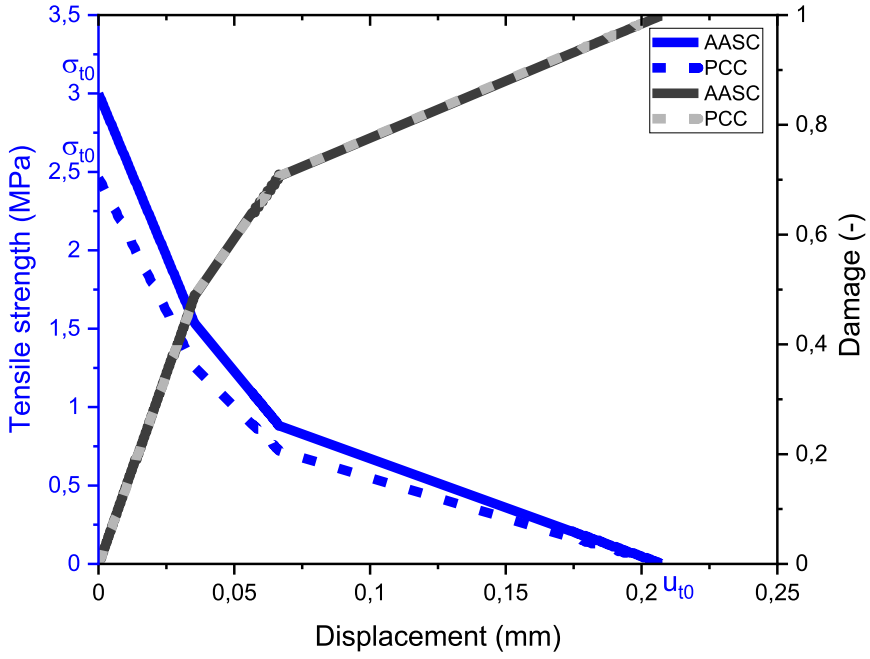

Fig. 6. Trilinear softening (blue) and damage (black) laws implemented in the CDP model to describe the post-cracking behaviour of both AASC and PCC. (For interpretation of the references to colour in this figure legend, the reader is referred to the Web version of this article.)

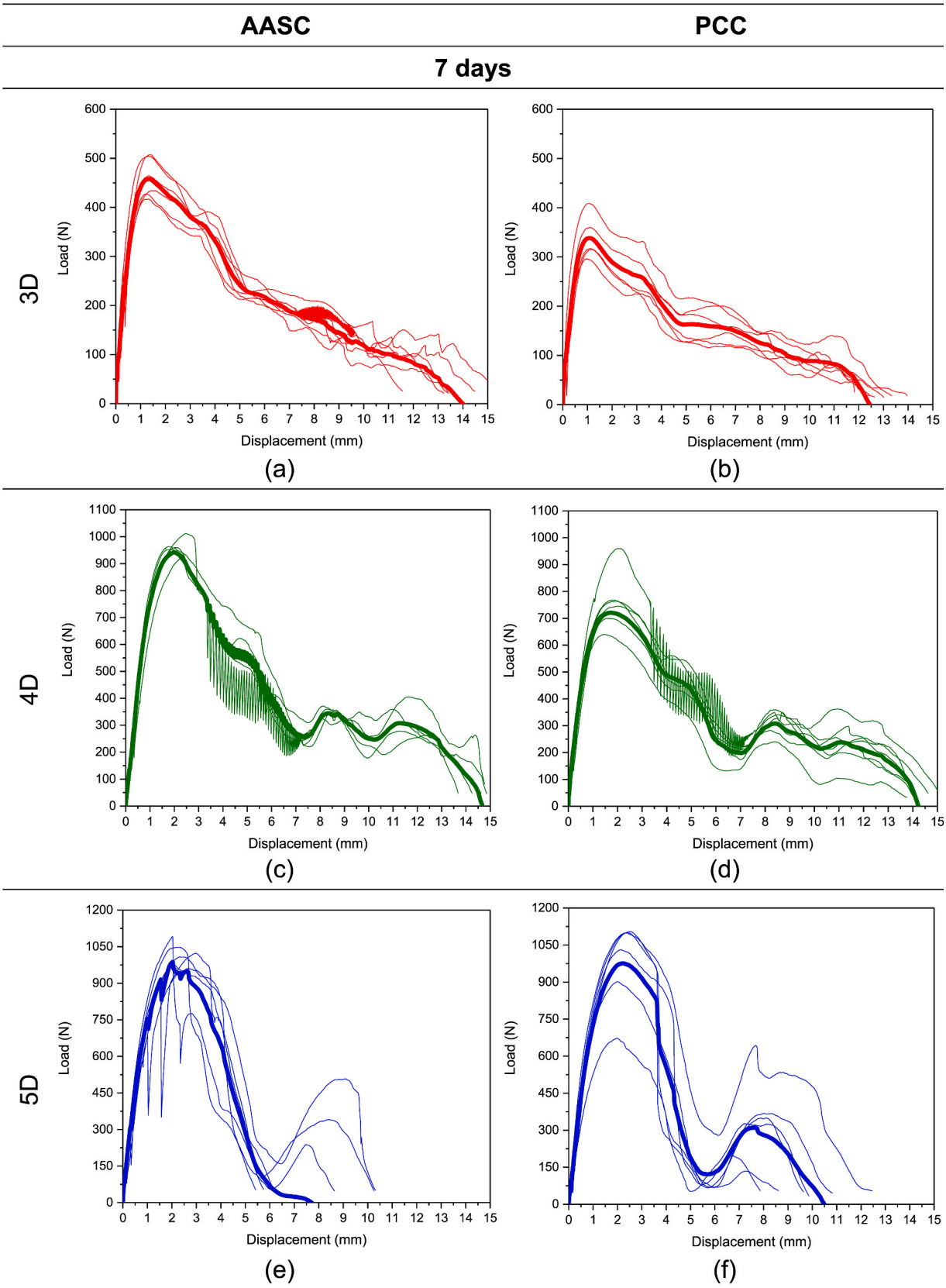

Fig. 7. Experimental pull-out curves for AASC and PCC incorporating (a – b, g – h) 3D, (c – d, i – j) 4D and (e – f, k – l) 5D fibres after 7 and 28 days. The bold lines indicate the average experimental curves, obtained from six samples.

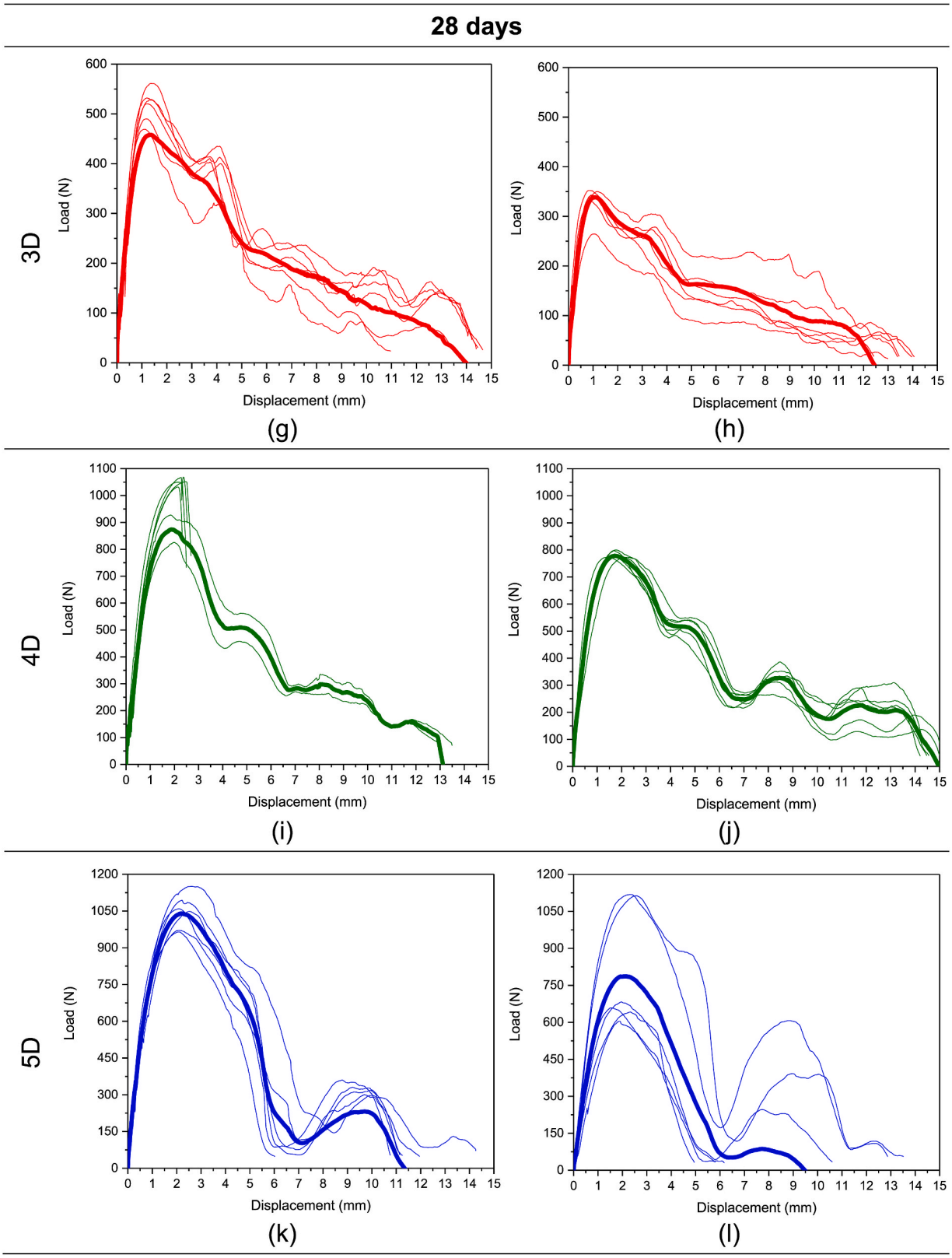

Fig. 7. (*continued*).

$$D = \frac{\delta_s^f \left(\delta_s - \delta_s^0\right)}{\delta_s \left(\delta_s^f - \delta_s^0\right)} \tag{9}$$

where δ_s^f is the separation at complete failure, and δ_s^0 is the separation at damage initiation. Since the fibre-matrix interface was implemented through cohesive surfaces in ABAQUS, both normal and tangential interaction properties had to be defined. To prevent surface interpenetration, a hard contact was assumed for the normal interaction, whereas for the tangential interaction a Coulomb friction model was adopted:

$$\tau_{crit} = \mu^* p \quad (10)$$

where τ_{crit} is the critical shear stress that initiates sliding, μ is the friction coefficient, and p is the normal contact pressure between the surfaces. This modelling strategy allows the fibre pull-out process to be fully described: Stages I-IV (debonding and slippage) are governed by the cohesive law, while Stage V (frictional sliding) is governed by the Coulomb friction model once complete fibre-matrix debonding has occurred (Fig. 1).

To determine the required parameters for the CZM – namely K_s, t_s^0 and δ_s^f – as well as the friction coefficient μ, a numerical inverse analysis was performed using the differential evolution algorithm implemented in the SciPy package [34]. Differential evolution is a stochastic, gradient-free evolutionary algorithm that is well suited for non-linear and non-differentiable objective functions with multiple local minima. The algorithm iteratively improves a population of candidate solutions through evolutionary computing principles (mutation, recombination, and selection mechanisms). The optimisation parameters included a maximum number of 1000 generations and a relative convergence tolerance of 0.01. Convergence was assumed when the standard deviation of the objective function values within the population fell below the specified tolerance. The objective function was defined as the sum of absolute differences between experimentally measured and numerically predicted pull-out load values. Linear interpolation was applied to both experimental and numerical pull-out load-displacement curves to ensure a consistent comparison. The optimisation was carried out using the average experimental curves shown in Figs. 7 and 8. Parameters bounds for the optimisation were selected from the literature [3], [19], [33]: $K_{ss} \in$ [4.5 N/mm, 55 N/mm], $t_s^0 \in$ [0.1 MPa, 3 MPa], $\delta_s \in$ [0.7 mm, 3 mm], and $\mu \in$ [0.08, 0.5].

3. Results

3.1. Effect of matrix type and strength

The experimental pull-out load-displacement curves for AASC and PCC incorporating 3D, 4D and 5D fibres at 7 and 28 days are presented in Figs. 7 and 8. The overall shape of the pull-out response is similar across all fibre types and matrix systems, regardless of curing age. Up to the maximum pull-out peak load, progressive debonding of the fibre from the concrete matrix occurs. Following peak load, unstable fibre-matrix debonding leads to a drop in pull-out force, while subsequent load fluctuations (e.g. Fig. 7c) are mainly associated with progressive straightening of the hooked-ends, as well as evolving frictional resistance as the fibre slides within the matrix channel. Once the fibre-matrix debonding is complete, the pull-out response is governed by plastic deformation of the hooked ends resulting in multiple load peaks as the force decreases until complete fibre slippage. In some cases – specifically for 4D fibres embedded in AASC at 28 days (Fig. 7i) – fibre rupture was observed due to the higher pull-out loads achieved.

For both AASC and PCC, the variability in test results increases with the complexity of the fibre geometry (5D > 4D > 3D). This is likely due to geometrical inconsistencies in the fibre hooks [35] and localised differences in porosity and micro-defects around the fibres, which are more pronounced for intricate geometries. Despite the relatively high scatter in the experimental data, fibres embedded in AASC generally exhibit higher peak and residual pull-out loads at both ages compared to those embedded in PCC. This enhanced performance in AASC can be attributed to the higher shrinkage of the concrete matrix, which induces compressive hydrostatic pressure at the fibre-matrix interface, strengthening the mechanical interlock and bond [16]. Additionally, AASC typically develops a denser fibre-matrix interfacial transition zone (ITZ) and a more compact microstructure due to lower porosity compared to cement-based matrices [5].

Fig. 8 provides a direct comparison between the different fibre types embedded in both AASC and PCC at 7 and 28 days. In AASC (Fig. 8a and b), all fibre types display similar pull-out responses at both ages, with 5D fibres outperforming 4D and 3D fibres (5D > 4D > 3D). Although the compressive strength of the alkali-activated slag-based concrete matrix increases of 37.2% from 7 to 28 days, its effect on the maximum pull-out load and post-peak response is limited. A similar trend can be observed in PCC: despite a 19.9% increase in compressive strength from 7 to 28 days, the single-fibre pull-out response remains largely unchanged for all fibre types, with 5D fibres again showing superior performance, albeit with the highest variability.

3.2. Effect of fibre geometry

As shown in Figs. 7 and 8, the maximum pull-out load increases with the number of bends at the fibre ends for both AASC and PCC at 7 and 28 days. The area under the load-displacement curves represents the energy absorbed during fibre debonding and pull-out. A significant portion of this energy is dissipated during debonding and plastic deformation of the fibre hooks, due to the enhanced mechanical anchorage provided by

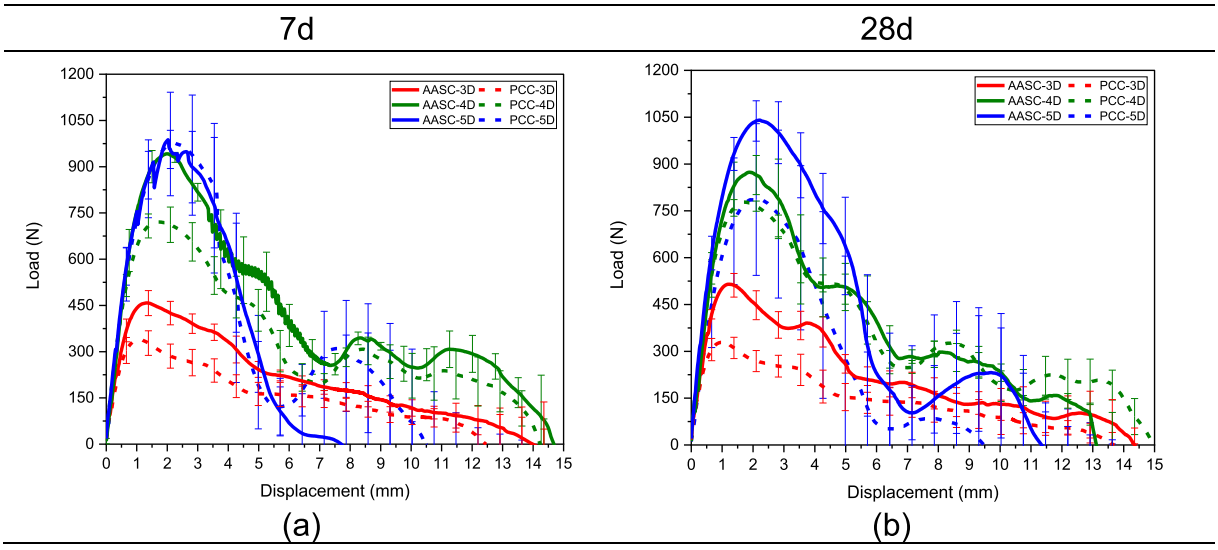

Fig. 8. Comparison of the experimental pull-out curves for 3D, 4D and 5D fibres embedded in AASC and PCC at (a) 7 and (b) 28 days. Each bold line indicate the average experimental curves, obtained from six samples.

the additional bends. Consequently, total energy absorption generally increases with the number of bends (5D > 4D > 3D), with AASC consistently showing higher values than PCC. Furthermore, 5D fibres show a more abrupt drop in pull-out load after reaching the peak load compared to 3D and 4D in both matrices.

Tables 7 and 8 summarise the maximum pull-out load (P_{max}), the average and equivalent bond strength (τ_{avg} and τ_{eqv}, respectively), and the fibre material utilisation factor (*FMUF*) for each fibre and concrete matrix type at 7 and 28 days. Together with the value of P_{max} of the average curve, the minimum and the maximum value of P_{max} observed for each series of samples is given. As observed in Fig. 9a and b, both the maximum pull-out load and the average bond strength increase with the number of bends, with 5D fibres achieving the highest values, albeit with greater variability in PCC mixes. Interestingly, for both AASC and PCC, 4D fibres exhibit the highest equivalent bond strength and *FMUF* values close to 1 (Fig. 9c and d), indicating that they make the most efficient use of the fibre material despite slightly lower peak loads than 5D fibres.

A similar trend was reported by Shaikh [5], who observed that P_{max}, τ_{avg}, τ_{eqv} and *FMUF* generally increase with the number of bends at the fibre ends in various mortar matrices, including fly ash-based alkali-activated mortar, fly ash-slag alkali-activated mortar, and cement-based mortar. Notably, the highest *FMUF* values were obtained for 4D fibres in both fly ash-based and cement-based mortars, which aligns with the present findings for AASC and PCC. This indicates that, although 5D fibres generally achieve higher peak and average bond strengths due to their more complex geometry, 4D fibres allow the material to be used at its maximum potential, as reflected by their superior *FMUF*. Therefore, the combination of the concrete matrix properties with the geometry and tensile strength of 4D fibres provides the optimal configuration to fully exploit the fibre's potential.

The pull-out performance of hooked-end steel fibres depends not only on fibre geometry but also on the properties of the concrete matrix and the fibre-matrix bond strength. A fibre can achieve its full potential only when embedded in a matrix with suitable characteristics – such as optimal microstructure and strength – that allow the fibre geometry to be effectively engaged. Although 5D fibres can achieve higher bond strength, their hooks may not be fully exploited in either matrices, whereas 4D fibres consistently provide the most efficient material utilisation in both AASC and PCC.

3.3. Numerical modelling

As minimal differences can be seen between the experimental results at 7 and 28 days, only the 28-day numerical load-displacement curves obtained through inverse analysis for AASC and PCC for each fibre type are shown in Fig. 10. For AASC, the numerical results accurately capture the experimental pull-out behaviour for all fibre geometries. Specifically, both the numerical peak load and the post-peak descending branch fall within the range of the experimental data. For PCC, the numerical curves generally align with the experimental results for all fibre types, although an overestimation of the peak load can be observed for 3D fibres (Fig. 10b). This discrepancy may be attributed to the model's limitations in accounting for micro-scale heterogeneities at fibre-matrix interface, which significantly influence the pull-out response. Importantly, in all cases, the fibre deformation at the end of the numerical pull-out process matches the experimental observations.

The fibre deformation corresponding to the maximum pull-out load (P_{max}), the plastic hinges (H_1, H_2, H_3, H_4) formation and the ultimate pull-out load (P_u) are given for each fibre type and concrete matrix in the supplementary information (Figure A.1 – A.6). Table 9 summarises the fibre-matrix interface parameters (K_{ss}, t_{ss}, δ_s^f, and μ) obtained through inverse analysis at 28 days for both concrete matrices and each fibre type.

As shown in Table 9, both AASC and PCC exhibit similar fibre-matrix interface parameters overall. K_{ss} (interface stiffness) is directly linked to the initial slope of the load-displacement curve and it increases with the number of bends at the end of the fibre, with 5D fibres showing the highest values of K_{ss} for both AASC and PCC. The additional bends provide additional mechanical anchorage, which explains why 5D fibres show higher load values for the same displacement in comparison to 3D and 4D fibres, resulting in a steeper initial linear branch of the curve. The opposite trend can be observed for δ_s^f, which decreases with the increase in number of bends at the fibre ends for both AASC and PCC. This behaviour may be related to the fact that the CDP model allows for stress redistribution around the fibre-matrix interface during all stages (Stage I – V) of the pull-out process.

The parameter t_{ss} (peak shear stress) is directly related to the peak of the pull-out load-displacement curve, so higher values of t_{ss} correspond to stronger fibre-matrix bonding. The highest values of t_{ss} are observed for 4D fibres embedded in both AASC and PCC, correlating well with the highest fibre material utilisation factor observed for this fibre type in this study. Regarding the friction coefficient μ, similar values are observed for both concrete types. This similarity can be attributed to the use of the CDP model for the concrete matrix, which allows for stress redistribution around the fibre-matrix interface during the pull-out process, thereby reducing the influence of friction in the final stage of the pull-out process (Stage V, Fig. 1).

The fibre-matrix bond fracture energy G_F, represented by the area under the $t_{ss} - \delta_s^f$ curve, was also calculated. The values of the fibre-matrix bond fracture energy for both AASC and PCC and for each fibre type at 28 days are listed in Table 10.

Although 4D fibres exhibit the highest fibre material utilisation factor in both AASC and PCC, this corresponds to the highest value of fibre-matrix bond fracture energy only in PCC. In AASC, the fibre-matrix bond fracture energy decreases with the number of bends at the fibre ends. The higher fibre-matrix bond fracture energy observed for 3D fibres in AASC can be explained by the combination of slightly lower t_{ss} for 3D fibres compared to 4D fibres and larger separation at failure δ_s^f,

Table 7
Values of P_{max}, τ_{avg}, τ_{eqv}, and *FMUF* for AASC and PCC at 7 days.

Fibre type	P_{max} [N]			τ_{avg} [MPa]		τ_{eqv} [MPa]		*FMUF*	
		AASC	PCC	AASC	PCC	AASC	PCC	AASC	PCC
3D 65/60 BG	avg	458.1	338.4	10.8 (0.9)	8.0 (0.9)	9.45 (0.93)	6.58 (1.13)	0.62 (0.05)	0.46 (0.05)
	min	416.9	296.4						
	max	507.3	408.7						
4D 65/60 BG	avg	941.7[a]	720.5	22.6 (0.7)	17.1 (1.0)	19.65 (1.72)	15.54 (2.32)	0.94 (0.03)	0.71 (0.05)
	min	917.3	639.3						
	max	1012.2	767.2						
5D 65/60 BG	avg	987.3	975.8	24.0 (1.0)	23.3 (3.7)	12.90 (2.96)	14.21 (4.22)	0.70 (0.03)	0.67 (0.12)
	min	960.3	673.5						
	max	1091.2	1104.4						

[a] The experimental curves in which fibre rupture was observed were not considered for the determination of the average curve, but only for the determination of the min and max values.

Table 8
Values of P_{max}, τ_{avg}, τ_{eqv}, and *FMUF* for AASC and PCC at 28 days.

Fibre type	P_{max} [N]			τ_{avg} [MPa]		τ_{eqv} [MPa]		*FMUF*	
		AASC	PCC	AASC	PCC	AASC	PCC	AASC	PCC
3D 65/60 BG	avg	514.9	328.8	12.2 (0.7)	7.8 (0.7)	10.11 (1.82)	6.54 (1.65)	0.70 (0.04)	0.45 (0.04)
	min	469.1	264.5						
	max	561.2	352.3						
4D 65/60 BG	avg	873.8[a]	778.1	23.4 (2.1)	18.5 (0.27)	10.31 (5.85)	17.15 (1.33)	0.97 (0.09)	0.77 (0.01)
	min	825.7	772.4						
	max	1068.3	800.0						
5D 65/60 BG	avg	1040.4	786.7	24.7 (1.5)	18.9 (5.2)	17.35 (3.81)	12.45 (8.05)	0.72 (0.05)	0.55 (0.17)
	min	964.7	604.5						
	max	1150.7	1118.6						

[a] The experimental curves in which fibre rupture was observed were not considered for the determination of the average curve, but only for the determination of the min and max values.

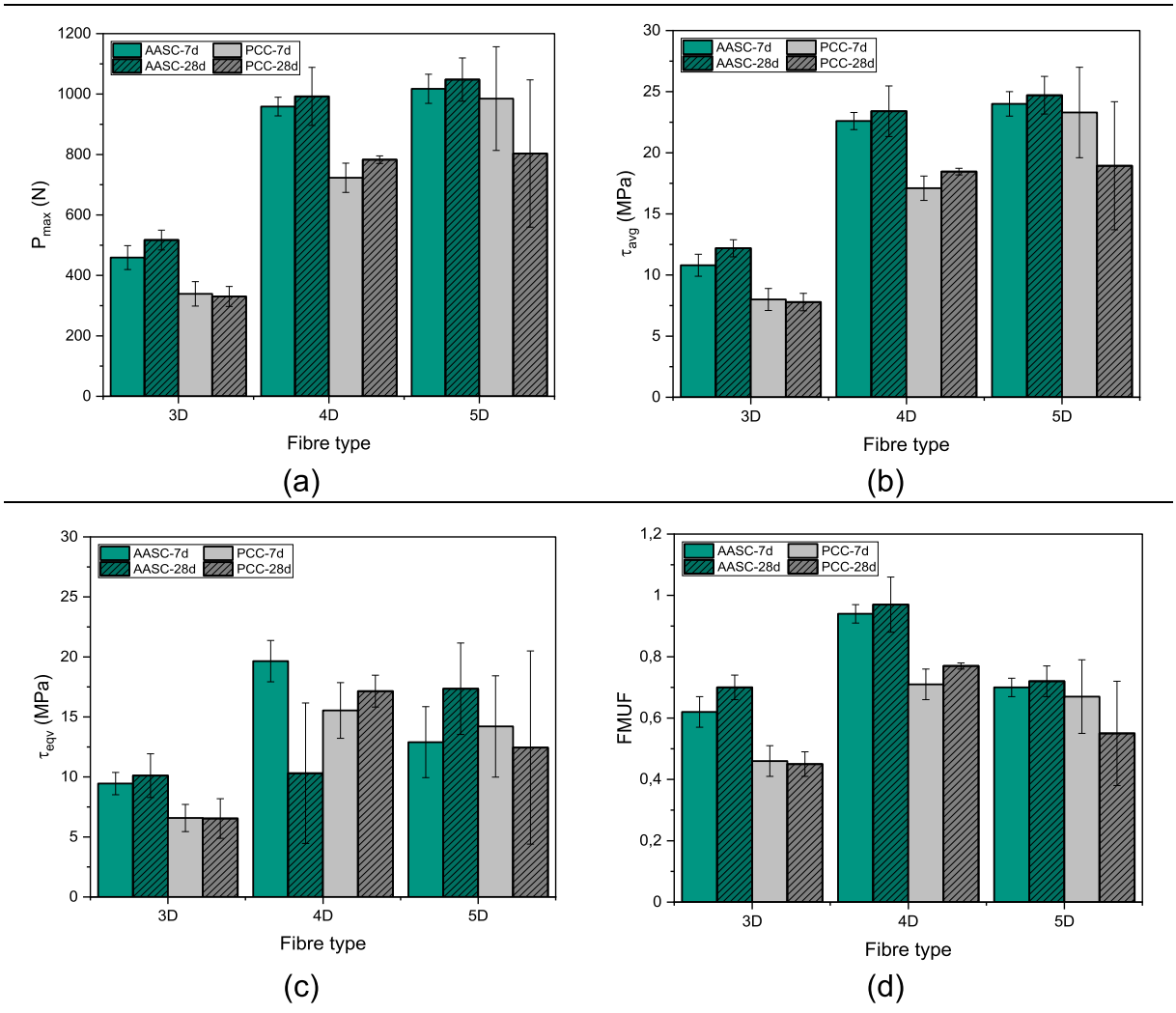

Fig. 9. Comparison between the values of (a) P_{max}, (b) τ_{avg}, (c) τ_{eqv}, and (d) *FMUF* for AASC and PCC at both 7 and 28 days.

resulting in a higher total fibre-matrix bond fracture energy for 3D fibres in AASC. Therefore, 4D fibres achieve their full-strength capacity primarily at completed pull-out, while 5D fibres, despite higher peak loads, do not fully exploit their potential energy absorption in either concrete matrices.

3.4. Correlation between pull-out response and flexural behaviour

Once the number of fibres at the beam cross-section (N_f) and the average fibre-matrix bond strength (τ_{avg}) are known for each fibre type and concrete matrix, a correlation can be established between the single-fibre pull-out response and the residual flexural strengths f_{R1} and f_{R3} summarised in Table 4, as shown in Fig. 11.

A linear regression analysis was performed separately for each fibre and concrete matrix. The relationship was modelled using the general formula $y = A{\cdot}x$, where y represents the residual flexural strengths f_{R1} and f_{R3}, and $x = \tau_{avg}{\cdot}N_f$. The coefficient A and the coefficient of deter-

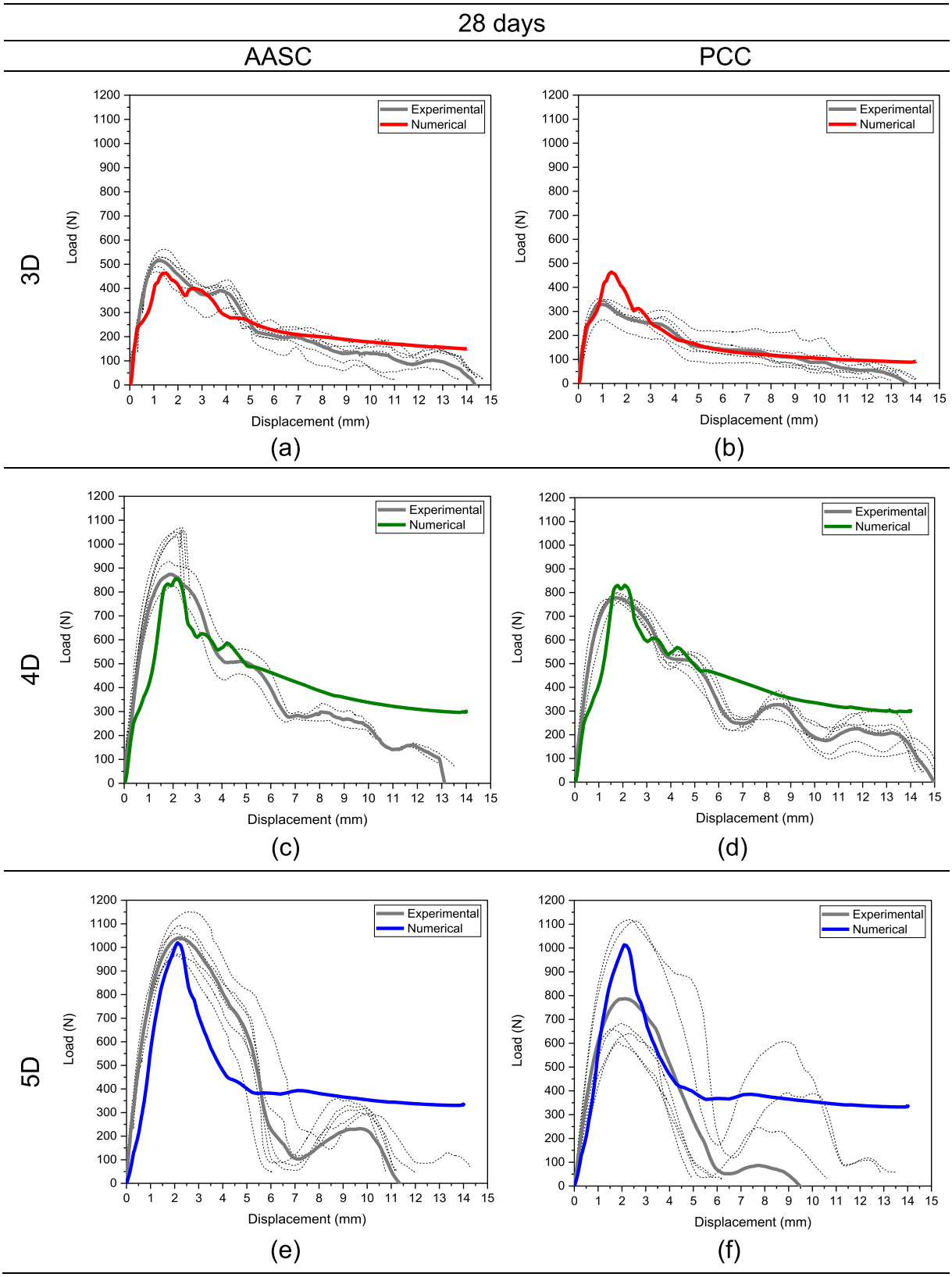

Fig. 10. Experimental and numerical pull-out load-displacement curves for AASC and PCC incorporating (a, b) 3D, (c, d) 4D, and (e, f) 5D fibres at 28 days.

mination R^2 for each case are summarised in Table 11.

As shown in Figs. 11, 4D and 5D fibres exhibit similar behaviour in both AASC and PCC. In contrast, 3D fibres display the highest values of coefficient A, resulting in a steeper slope for the linear fit. This indicates that, although τ_{avg} increases with the number of bends at the fibre ends (5D > 4D > 3D), a higher number of 3D fibres is required to achieve the same residual flexural strength (f_{R1} or f_{R3}) as 4D or 5D fibres. Therefore, higher dosages of 3D fibres are necessary to achieve similar mechanical

Table 9
Fibre-matrix interface parameters obtained through inverse analysis at 28 days.

Parameter	AASC			PCC		
	3D	4D	5D	3D	4D	5D
K_{ss} [N/mm]	4.51	35.36	40.80	4.52	35.16	40.77
t_{ss} [MPa]	0.80	1.74	1.16	0.32	2.04	0.16
δ_s^f [mm]	2.66	1.13	0.94	2.01	1.01	1.02
μ [−]	0.20	0.10	0.10	0.10	0.10	0.10

Table 10
Values of the fibre-matrix bond fracture energy G_F [kN/m] at 28 days.

Matrix	3D	4D	5D
AASC	1.064	0.983	0.545
PCC	0.322	1.030	0.082

performance. The similar behaviour between 4D and 5D fibres in both AASC and PCC may be attributed to the incompatibility between the enhanced potential of the 5D fibres and the compressive strength of the concrete matrix, which ultimately limits the performance of 5D fibres relative to their theoretical potential.

4. Conclusions

This study experimentally investigates the single-fibre pull-out behaviour of single and multiple hooked-end steel fibres (3D, 4D and 5D) embedded in two types of concrete matrix: alkali-activated slag-based concrete (AASC) and Portland cement-based concrete (PCC). A finite element model-based inverse analysis was employed to derive the

Table 11
Values of the coefficient A and R^2 for each fibre and concrete matrix type.

		AASC			PCC		
		3D	4D	5D	3D	4D	5D
f_{R1}	A	0.0039	0.0024	0.0022	0.0071	0.0033	0.0038
	R^2	0.973	0.974	0.966	0.954	0.914	0.897
f_{R3}	A	0.0045	0.0026	0.0025	0.0081	0.0040	0.0043
	R^2	0.969	0.941	0.951	0.966	0.904	0.929

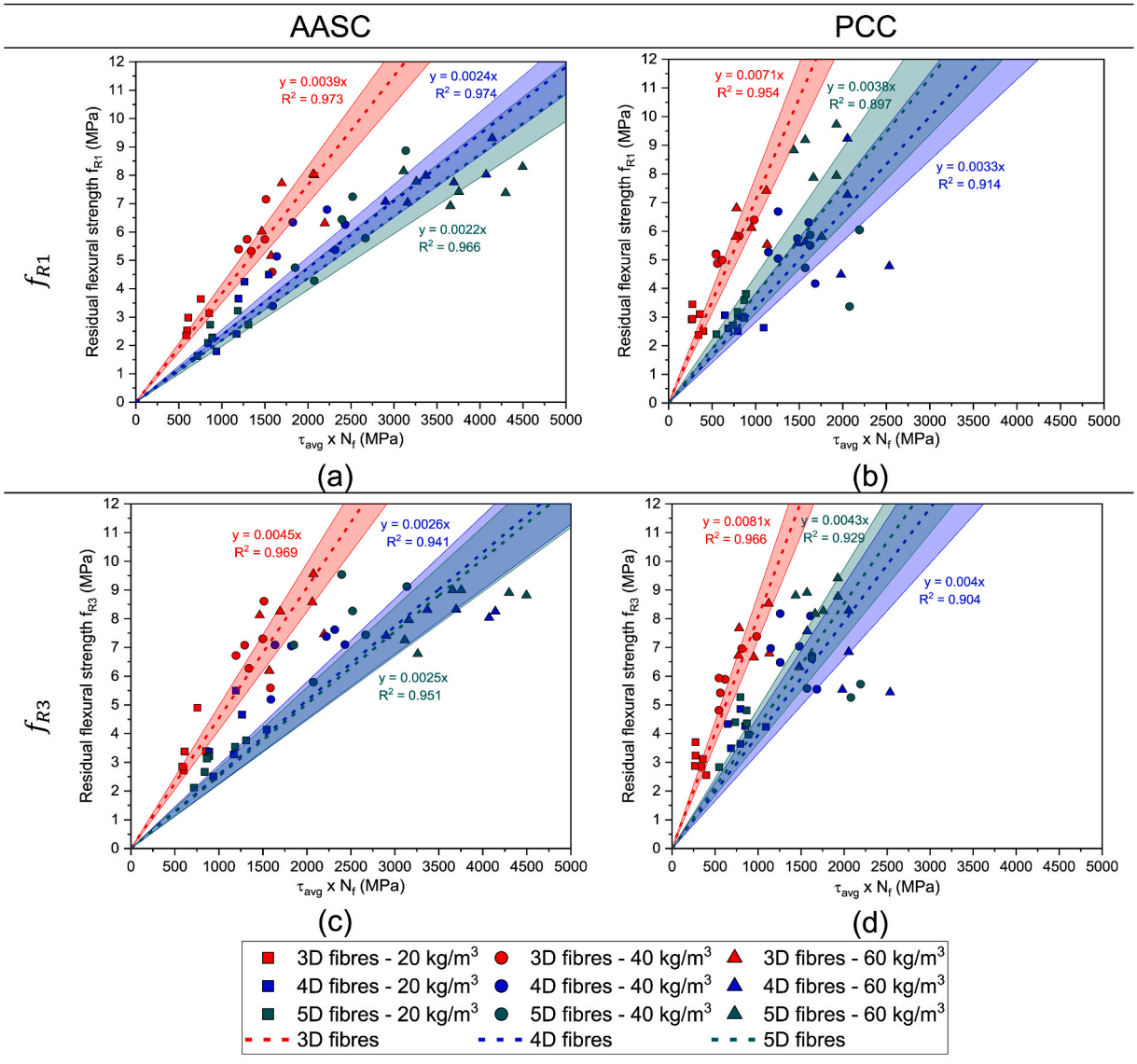

Fig. 11. Correlation between the number of fibres and the fibre-matrix bond strength and the residual flexural strength (a, b) f_{R1} and (c, d) f_{R3} for AASC and PCC mixes.

key fibre-matrix interface parameters for the use in the Cohesive Zone Model (CZM) in ABAQUS. Based on the experimental results and numerical modelling, the following conclusions can be drawn:

- ***Effect of the matrix type:*** The compressive strength of the concrete matrix has a marginal effect on the maximum pull-out load and the post-peak response for each fibre type when comparing results at 7 and 28 days. However, fibres embedded in AASC consistently exhibit higher maximum pull-out loads than those in PCC, likely due to the stronger fibre-matrix bond in AASC, which may be enhanced by its higher shrinkage compared to PCC.
- ***Effect of the fibre geometry:*** Fibre geometry, specifically the number of bends at the fibre ends, has a more significant impact on the peak pull-out load and post-peak behaviour at 7 and 28 days. For both matrix types, the maximum pull-out load (P_{max}) and the average bond strength (τ_{avg}) increase with the increase of the number of bends at the fibre ends (5D > 4D > 3D). In contrast, the equivalent bond strength (τ_{eqv}) and the fibre material utilisation factor (*FMUF*) are highest for 4D fibres (4D > 5D > 3D). This indicates an optimal compatibility between the matrix properties (e.g., compressive strength) and the fibre characteristics (geometry and tensile strength), allowing the fibre to be fully utilised.
- ***Correlation between bond strength and flexural behaviour:*** The fibre-matrix average bond strength (τ_{avg}) increases with the number of bends at the fibre ends (5D > 4D > 3D). When correlated with the number of fibres in the cross-section of beams tested under three-point bending tests (N_f), a linear relationship is observed with the post-cracking residual flexural tensile strengths f_{R1} and f_{R3}. While 3D fibres exhibit lower τ_{avg} values, their higher fibre count can result in comparable or even higher flexural strengths, indicating that higher dosages of 3D fibres are required to match the performance of 4D and 5D fibres.
- ***Numerical model parameters:*** The interface parameters obtained through inverse analysis correspond to different stages of the pull-out load-displacement curve. Specifically, K_{ss} and t_{ss} govern the initial debonding stage, influencing the initial slope of the curve up to the maximum pull-out load. K_{ss} increases with the number of bends at the end of the fibre, with 5D fibres showing the highest values for both AASC and PCC. The additional bends enhance the fibre mechanical anchorage, which explains why 5D fibres can sustain higher loads at same displacement compared to 3D and 4D fibres, resulting in a steeper initial linear branch of the load-displacement curve. Conversely, δ_s^f decreases as the number of bends at the end of the fibre increases for both AASC and PCC. This behaviour can be attributed to the formation of additional inelastic hinges during the pull-out process, which delay the fibre failure. Furthermore, the highest values of t_{ss} are obtained for 4D fibres for both AASC and PCC, aligning with the highest fibre material utilisation factor observed for this fibre type in this study. The fibre-matrix interface parameters obtained through inverse analysis can be employed in meso-scale models to predict the mechanical behaviour of SFRAASC, thereby enabling more accurate simulations of its structural performance.
- ***Fibre-matrix bond fracture energy and FMUF:*** Among all fibres, 4D fibres embedded in both AASC and PCC exhibit the highest fibre-matrix bond fracture energy, which can be attributed to their superior fibre material utilisation factor (*FMUF*) observed in this study.

CRediT authorship contribution statement

Laura Rossi: Writing – original draft, Validation, Methodology, Investigation, Formal analysis, Conceptualization. **Maria Paula Zappitelli:** Writing – original draft, Visualization, Software, Methodology, Formal analysis, Conceptualization. **Ravi A. Patel:** Writing – review & editing, Supervision, Methodology, Formal analysis, Conceptualization. **Frank Dehn:** Writing – review & editing, Supervision, Resources, Funding acquisition.

Declaration of competing interest

The authors declare that they have no known competing financial interests or personal relationships that could have appeared to influence the work reported in this paper.

Acknowledgements

This project has received funding from the European Union's Horizon 2020 research and innovation programme under grant agreement No 813596 DuRSAAM. The opinions expressed in this document reflect only the author's view and reflect in no way the European Commission's opinions. The European Commission is not responsible for any use that may be made of the information it contains.

Appendix A. Supplementary data

Supplementary data to this article can be found online at https://doi.org/10.1016/j.cemconcomp.2026.106643.

Data availability

Data will be made available on request.

References

[1] C. Lin, T. Kanstad, S. Jacobsen, G. Ji, Bonding property between fiber and cementitious matrix: a critical review, Constr. Build. Mater. 378 (May 2023) 131169, https://doi.org/10.1016/j.conbuildmat.2023.131169.
[2] S. Abdallah, M. Fan, D.W.A. Rees, Predicting pull-out behaviour of 4D/5D hooked end fibres embedded in normal-high strength concrete, Eng. Struct. 172 (Oct. 2018) 967–980, https://doi.org/10.1016/j.engstruct.2018.06.066.
[3] Y.M. Abbas, Microscale cohesive-friction-based finite element model for the crack opening mechanism of hooked-end steel fiber-reinforced concrete, Materials 14 (3) (Feb. 2021) 669, https://doi.org/10.3390/ma14030669.
[4] F. Deng, X. Ding, Y. Chi, L. Xu, L. Wang, The pull-out behavior of straight and hooked-end steel fiber from hybrid fiber reinforced cementitious composite: experimental study and analytical modelling, Compos. Struct. 206 (Dec. 2018) 693–712, https://doi.org/10.1016/j.compstruct.2018.08.066.
[5] F.U.A. Shaikh, Pullout behavior of hook end steel fibers in geopolymers, J. Mater. Civ. Eng. 31 (6) (Jan. 2019) 04019068, https://doi.org/10.1061/(ASCE)MT.1943-5533.0002722.
[6] G. Chen, D. Gao, H. Zhu, J. Song Yuan, X. Xiao, W. Wang, Effects of novel multiple hooked-end steel fibres on flexural tensile behaviour of notched concrete beams with various strength grades, Structures 33 (Jan. 2021) 3644–3654, https://doi.org/10.1016/j.istruc.2021.06.016.
[7] L. Rossi, M.P. Zappitelli, R.A. Patel, F. Dehn, Flexural tensile behaviour of alkali-activated slag-based concrete and Portland cement-based concrete incorporating single and multiple hooked-end steel fibres, J. Build. Eng. 98 (Dec. 2024) 111090, https://doi.org/10.1016/j.jobe.2024.111090.
[8] S. Abdallah, M. Fan, D.W.A. Rees, Analysis and modelling of mechanical Anchorage of 4D/5D hooked end steel fibres, Mater. Des. 112 (Jan. 2016) 539–552, https://doi.org/10.1016/j.matdes.2016.09.107.
[9] I. Löfgren, *Fibre-reinforced concrete for industrial construction: a fracture mechanics approach to material testing and structural analysis*, vol. N.S., 2378, in: Doktorsavhandlingar Vid Chalmers Tekniska Högskola, vol. N.S., Chalmers Univ. of Technology, Göteborg, 2005, p. 2378.
[10] S. Abdallah, M. Fan, X. Zhou, S. Le Geyt, Anchorage effects of various steel fibre architectures for concrete reinforcement, Int. J. Concr. Struct. Mater. 10 (3) (Jan. 2016) 325–335, https://doi.org/10.1007/s40069-016-0148-5.
[11] D.-Y. Yoo, J.-J. Park, S.-W. Kim, Fiber pullout behavior of HPFRCC: effects of matrix strength and fiber type, Compos. Struct. 174 (Aug. 2017) 263–276, https://doi.org/10.1016/j.compstruct.2017.04.064.
[12] S. Abdallah, Mizi Fan, Xiangming Zhou, Effect of hooked-end steel fibres geometry on pull-out behaviour of Ultra-, High Performance Concrete' (Nov. 2016), https://doi.org/10.5281/ZENODO.1128020.
[13] S. Abdallah, D.W.A. Rees, S.H. Ghaffar, M. Fan, Understanding the effects of hooked-end steel fibre geometry on the uniaxial tensile behaviour of self-compacting concrete, Constr. Build. Mater. 178 (Jan. 2018) 484–494, https://doi.org/10.1016/j.conbuildmat.2018.05.191.
[14] S. Abdallah, M. Fan, X. Zhou, Pull-out behaviour of hooked end steel fibres embedded in ultra-high performance mortar with various W/B ratios, Int. J. Concr. Struct. Mater. 11 (2) (Jan. 2017) 301–313, https://doi.org/10.1007/s40069-017-0193-8.

[15] F.U.A. Shaikh, Y. Shafaei, P.K. Sarker, Effect of nano and micro-silica on bond behaviour of steel and polypropylene fibres in high volume fly ash mortar, Constr. Build. Mater. 115 (Jan. 2016) 690–698, https://doi.org/10.1016/j.conbuildmat.2016.04.090.
[16] A. Beglarigale, S. Aydın, C. Kızılırmak, Fiber-matrix bond characteristics of alkali-activated slag cement–based composites, J. Mater. Civ. Eng. 28 (11) (Nov. 2016) 04016133, https://doi.org/10.1061/(ASCE)MT.1943-5533.0001642.
[17] E. Poveda, R.C. Yu, M. Tarifa, G. Ruiz, V.M.C.F. Cunha, J.A.O. Barros, Rate effect in inclined fibre pull-out for smooth and hooked-end fibres: a numerical study, Int. J. Fract. 223 (1–2) (May 2020) 135–149, https://doi.org/10.1007/s10704-019-00404-7.
[18] A.P. Fantilli, P. Vallini, A cohesive interface model for the pullout of inclined steel fibers in cementitious matrixes, J. Adv. Concr. Technol. 5 (2) (2007) 247–258, https://doi.org/10.3151/jact.5.247.
[19] Z. Zou, M. Hameed, Combining interface damage and friction in cohesive interface models using an energy based approach, Compos. Part Appl. Sci. Manuf. 112 (Sep. 2018) 290–298, https://doi.org/10.1016/j.compositesa.2018.06.017.
[20] M. Manca, A. Karrech, P. Dight, D. Ciancio, Dual cohesive elements for 3D modelling of synthetic fibre-reinforced concrete, Eng. Struct. 174 (Nov. 2018) 851–860, https://doi.org/10.1016/j.engstruct.2018.07.101.
[21] H. Wang, Y. Jiang, L. Liu, Meso-mechanical simulation of the mechanical behavior of different types of steel fibers reinforced concretes, Sustainability 14 (23) (Nov. 2022) 15803, https://doi.org/10.3390/su142315803.
[22] G. Wu, H. Wang, Numerical simulation of steel fiber pull-out process based on cohesive zone model and unified phase-field theory, Sustainability 15 (5) (Feb. 2023) 4015, https://doi.org/10.3390/su15054015.
[23] B. Banholzer, W. Brameshuber, W. Jung, Analytical evaluation of pull-out tests—The inverse problem, Cem. Concr. Compos. 28 (6) (Jul. 2006) 564–571, https://doi.org/10.1016/j.cemconcomp.2006.02.015.
[24] I. Kožar, N. Torić Malić, D. Simonetti, Ž. Smolčić, Bond-slip parameter estimation in fiber reinforced concrete at failure using inverse stochastic model, Eng. Fail. Anal. 104 (Oct. 2019) 84–95, https://doi.org/10.1016/j.engfailanal.2019.05.019.
[25] D. Dupont, L. Vandewalle, Distribution of steel fibres in rectangular sections, Cem. Concr. Compos. 27 (3) (Mar. 2005) 391–398, https://doi.org/10.1016/j.cemconcomp.2004.03.005.
[26] T. Jankowiak, T. Łodygowski, Identification of parameters of concrete damage plasticity constitutive model, Found. Civ. Environ. Eng. 6 (Jan. 2005) 53–69.
[27] J. Lee, G.L. Fenves, Plastic-damage model for cyclic loading of concrete structures, J. Eng. Mech. 124 (8) (Jan. 1998) 892–900, https://doi.org/10.1061/(ASCE)0733-9399(1998)124:8(892).
[28] J. Lubliner, J. Oliver, S. Oller, E. Oñate, A plastic-damage model for concrete, Int. J. Solid Struct. 25 (3) (Jan. 1989) 299–326, https://doi.org/10.1016/0020-7683(89)90050-4.
[29] D.S. Dugdale, Yielding of steel sheets containing slits, J. Mech. Phys. Solid. 8 (2) (May 1960) 100–104, https://doi.org/10.1016/0022-5096(60)90013-2.
[30] G.I. Barenblatt, The mathematical theory of equilibrium cracks in brittle fracture, in: Advances in Applied Mechanics, 7, Elsevier, 1962, pp. 55–129, https://doi.org/10.1016/S0065-2156(08)70121-2.
[31] A. Rolland, P. Argoul, K. Benzarti, M. Quiertant, S. Chataigner, A. Khadour, Analytical and numerical modeling of the bond behavior between FRP reinforcing bars and concrete, Constr. Build. Mater. 231 (Jan. 2020) 117160, https://doi.org/10.1016/j.conbuildmat.2019.117160.
[32] M. Smith, ABAQUS/standard User's Manual, Version 6.9. Providence, RI: Simulia.
[33] H. Zhang, Y.J. Huang, Z.J. Yang, S.L. Xu, X.W. Chen, A discrete-continuum coupled finite element modelling approach for fibre reinforced concrete, Cement Concr. Res. 106 (Apr. 2018) 130–143, https://doi.org/10.1016/j.cemconres.2018.01.010.
[34] R. Storn, K. Price, Differential evolution - a simple and efficient heuristic for global optimisation over continuous spaces, J. Global Optim. 11 (4) (Jan. 1997) 341–359, https://doi.org/10.1023/A:1008202821328.
[35] F. Isla, G. Ruano, B. Luccioni, Analysis of steel fibers pull-out. Experimental study, Constr. Build. Mater. 100 (Dec. 2015) 183–193, https://doi.org/10.1016/j.conbuildmat.2015.09.034.